Received July 31, 2017, accepted August 24, 2017. Date of publication xxxx 00, 0000, date of current version xxxx 00, 0000.

Digital Object Identifier 10.1109/ACCESS.2017.2751964

INVITED PAPER

LTE for Public Safety Networks: Synchronization in the Presence of Jamming

AMR EL-KEYI[1], OKTAY ÜRETEN[2], HALIM YANIKOMEROGLU[1], (Fellow, IEEE), AND TREVOR YENSEN[2]

[1]Department of Systems and Computer Engineering, Carleton University, Ottawa, ON, Canada
[2]Allen-Vanguard Corporation, Ottawa, ON, Canada

Corresponding author: Halim Yanikomeroglu (halim.yanikomeroglu@sce.carleton.ca)

This work was supported by the National Sciences and Engineering Research Council of Canada Engage Program.

ABSTRACT In this paper, an algorithm for timing synchronization, cell identity detection, and carrier frequency offset (CFO) estimation is presented for long-term evolution (LTE) systems. The proposed algorithm is robust against partial-band interference and/or jamming. It utilizes adaptive filtering to suppress the contribution of the jamming signal to the timing detection metric without using any *a priori* knowledge of the jamming signal characteristics. The timing detection metric is computed by minimizing the output of the adaptive filter corresponding to any received signal that does not match the signature of the LTE primary synchronization signals (PSS). The filter coefficients are updated iteratively using the recursive least squares algorithm. The frequency response of the adaptive filter at the PSS detection instant is used to weight the contribution of different subcarriers to the metrics used in cell identity detection and CFO estimation. Simulation results are presented showing the ability of the proposed algorithm to complete the synchronization process successfully even in the presence of partial-band jamming signals that cover one third of the frequency band of the LTE synchronization signals.

INDEX TERMS LTE security, OFDM synchronization, adaptive interference and jamming cancellation.

I. INTRODUCTION

The long term evolution (LTE) standard is the primary standard for 4G cellular technology [1]. Compared to earlier cellular communication standards, LTE offers improved coverage, enhanced system capacity, higher spectral efficiency, lower latency, and higher peak data rates in a cost effective manner [2]. In addition to its commercial use, LTE has been selected as the technology for implementing First Responder Network Authority "FirstNet"; U.S.A's nationwide public-safety network [3]. Significant standardization activities have been conducted to address the requirements of operating broadband public-safety wireless networks using LTE [4]. These requirements include guaranteed access, reliability, and quality of service that ensure network coverage in various operating environments.

The first set of 5G standards, 3GPP Release 15, is currently under development including new radio access technologies in the mm-wave frequency band as well as LTE-Advanced Pro specifications [5]. Nevertheless, backward compatibility of Release 15 with LTE and LTE-advanced technology is expected in the current operating bands of LTE systems (below 6 GHz). Future 5G standards are expected to find application in numerous security-sensitive use cases, e.g., machine-type communication and vehicle-to-vehicle communication. As a result, improving the physical layer security of current 4G and future 5G wireless communication systems has recently received significant attention [6]–[8].

LTE systems are susceptible to interference [9], [10]. For example, field measurements have been reported confirming the presence of multiple narrowband systems causing interference to the uplink and downlink of LTE Band 31 (450-470 MHz) [11]. Interference is also expected in future evolution of LTE systems. For example, license-assisted access using LTE (LAA-LTE) operates in a spectrum that overlaps with Wi-Fi in the 5 GHz band [12]. Ensuring fair coexistence between LTE and Wi-Fi has been the principal focus of LAA standardization in LTE Release 13 [13], [14].

LTE systems are also sensitive to jamming. Denial of service jamming attacks that render the available resources of the LTE network inaccessible to the registered UEs can be accomplished by targeting the downlink control channels. The most vulnerable control channel in the LTE downlink is the Physical Downlink Control CHannel (PDCCH) that carries the downlink control information such as the resource schedules for downlink and uplink and transmission power commands. The vulnerability of the PDDCH was illustrated in [15] where simulation results were presented showing severe deterioration in the BER of the PDCCH decoder in some fading channels.

Jamming attacks against channel estimation algorithms for OFDM-based communication systems were discussed in [16]. In the LTE downlink signal, equal-power reference symbols (RS) are inserted in every resource block to enable the receiving user equipment (UE) to estimate the channel. Classical LTE channel estimation algorithms usually employ least squares to estimate the frequency response of the channel at the locations of the RS. Interpolation is then utilized to estimate the frequency response at the remaining time-frequency resource elements [17]. The effect of jamming the reference symbols on the performance of OFDM systems was investigated in [16] where it was shown that RS-jamming is 2 dB more efficient than barrage jamming.

Security challenges in LTE systems were discussed in [6]–[8]. In addition to control channels and RS jamming attacks, synchronization channel attacks were identified as one of the major threats to LTE systems. In order for a UE to join the LTE network, it has to acquire the frame timing information, estimate the carrier frequency offset (CFO), and identify the cell [18], [19]. The LTE downlink transmission contains two signals–the primary synchronization signal (PSS) and the secondary synchronization signal (SSS)–that are broadcasted to enable the user equipment (UE) to complete the synchronization and cell selection processes. Smart jamming attacks against LTE systems were investigated in [20] where experimental results were presented showing that targeting the LTE synchronization mechanism can cause permanent denial of service during the cell selection process.

Orthogonal frequency division multiplexing (OFDM)–the physical layer modulation for LTE downlink–is known for its sensitivity to timing and frequency synchronization errors [21]. Synchronization errors in OFDM systems destroy the orthogonality among the subcarriers resulting in severe degradation in the system performance. The sensitivity of conventional OFDM synchronization algorithms to partial-band interference was studied in [22] where the authors showed that the timing metric severely degrades as the power of the interference signal increases. The effect of inter-cell interference on the performance of LTE synchronization algorithms was also investigated in [18] where it was shown that LTE synchronization algorithms are interference limited.

Adaptive synchronization for OFDM-based powerline communication systems in the presence of narrowband interference was proposed in [23] where it was assumed that the interference signal has high temporal correlation while data samples separated by a duration longer than the channel delay spread are uncorrelated. An adaptive forward linear prediction error (FLPE) filter was used in [23] to estimate the interference signal using previous received samples. The estimated interference signal was then subtracted from the received signal to yield the output of the FLPE filter. Cross-correlation between the output of the FLPE filter and the reference synchronization symbol was used to compute the timing synchronization metric. However, the algorithm in [23] can cause partial cancellation of the information contained in the LTE synchronization signals leading to errors in cell identification and/or CFO estimation.

In this paper, we present an adaptive LTE synchronization algorithm with improved robustness against partial-band interference and/or jamming signals. To the best of our knowledge, this paper is the first paper to consider the problem of timing and/or frequency synchronization for LTE systems in the presence of interference or jamming. The proposed algorithm employs multiple parallel adaptive filters that eliminate the contribution of the interference signal to the timing metric. The coefficients of each adaptive filter are designed using the linearly constrained minimum variance (LCMV) criterion that minimizes the output power of the filter subject to constraints that preserve the received signal vectors corresponding to all possible PSS signatures. We convert the LCMV problem to an unconstrained optimization problem using the generalized sidelobe canceller (GSC) implementation. The adaptive GSC filter coefficients are updated iteratively using the recursive least squares (RLS) algorithm. The PSS detection metric is obtained from the outputs of the adaptive LCMV filters. The location of the PSS in the downlink frame can be estimated by searching for the maximum of the PSS detection metric over half the duration of the LTE downlink frame.

After locating the PSS, the proposed algorithm computes the weighted cross-correlation–in the frequency domain–between the received PSS vector and the PSS signatures. The magnitude frequency response of the LCMV filters at the PSS detection instant is used to weight the contribution of different subcarriers to the weighted cross-correlation metric. As a result, the contribution of the interference signal to the cross-correlation metric is eliminated. Weighted frequency-domain cross-correlation is also employed to jointly locate the SSS and decode its information. Hence, the receiver can obtain the duplexing and cyclic prefix (CP) modes of the system, the physical-layer cell identity and the frame timing information. Frequency synchronization is performed by processing the detected PSS and SSS in the frequency domain. We present numerical simulations that illustrate the ability of the proposed algorithm to effectively eliminate partial-band interference and jamming and synchronize to the LTE system even under high interference-to-signal ratio (ISR). It is worth mentioning that the proposed algorithm does not require any preliminary coarse synchronization, e.g., by searching for the CP, before processing the received signal in the frequency domain. Instead, using the proposed adaptive filtering algorithm, the location of the PSS can be determined even in the presence of interference or jamming. Afterwards, frequency-domain processing is used to eliminate the interference and decode the PSS. Our numerical results indicate that the proposed algorithm retains a high probability of detection even when the interference signal occupies one third of the bandwidth (BW) of the LTE synchronization signals.

The remainder of this paper is organized as follows. In Section II, we briefly review some relevant features of LTE downlink synchronization signals. In Section III, we present the proposed adaptive synchronization algorithm. Our numerical simulations are presented in Section IV and, finally, the paper is concluded in Section V.

II. LTE SYNCHRONIZATION SIGNALS

In this section, relevant characteristics of LTE downlink synchronization signals are reviewed with a focus on the frequency division duplex (FDD) mode of operation. The FDD downlink transmission is arranged in frames of 10 ms duration. Each frame is divided into ten subframes and each subframe consists of two slots of duration 0.5 ms. Each slot in turn consists of a number of OFDM symbols which can be either seven or six based on the CP mode. For the normal CP mode, the first symbol has a CP of length 5.2 μs while the remaining six symbols have a CP of length 4.69 μs. For the extended mode, CP duration is 16.67 μs for each OFDM symbol. The number of OFDM sub-carriers, $\bar{N}$, ranges from 128 to 2048, depending on the channel BW. The basic subcarrier spacing is 15 KHz, with a reduced subcarrier spacing of 7.5 KHz available for some transmission scenarios. For the 15 KHz spacing, the sampling rate is $f_s = 15\bar{N}$ KHz. In order to limit the overhead, downlink transmission is scheduled in units of resource blocks (RBs). Each RB consists of 12 consecutive sub-carriers and extends over the duration of 1 slot, i.e., each RB spans 180 KHz for the duration of 0.5 ms.

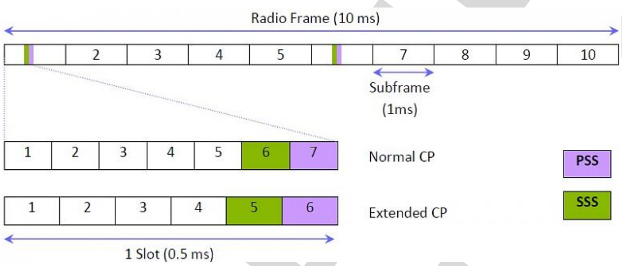

FIGURE 1. **Synchronization signals in LTE FDD downlink.**

Two synchronization signals–the PSS and SSS–are broadcasted in the LTE downlink. The UE utilizes these signals in timing and frequency synchronization. In addition, the synchronization signals enable the UE to acquire some system parameters such as the cell identity, the CP length, and the duplexing mode. The synchronization signals are transmitted twice in each 10 ms radio frame. Fig. 1 shows the location of the synchronization signals within the LTE FDD downlink frame. The PSS is located in the last OFDM symbol of the first and 11th slot of each radio frame which allows the UE to acquire the slot boundary timing independent of the type of CP. In the FDD mode, the OFDM symbol corresponding to the transmission of the SSS immediately precedes that corresponding to PSS transmission. In contrast, when time-division duplexing (TDD) is employed, the SSS is located 3 OFDM symbols ahead of the PSS [24]. The PSS and SSS occupy the central six RBs, irrespective of system BW, which allows the UE to synchronize to the network without *a priori* knowledge of its BW.

The PSS is constructed from a frequency-domain Zadoff-Chu (ZC) sequence of length 63, with the middle element punctured to avoid transmitting on the dc subcarrier. The length-63 ZC sequence with root r is given by

$$\mathrm{P}_r^{63}(n) = \exp\left(-j\frac{\pi rn(n+1)}{63}\right) \quad \text{for } n = 0, 1, \ldots, 62. \tag{1}$$

Three PSS sequences are used in LTE, corresponding to three physical-layer identities. The selected roots for the three ZC sequences are $r = 25, 29$, and 34 corresponding to physical-layer identities $N_{\mathrm{ID}}^{(2)} = 0, 1$, and 2, respectively.

Let $x_l(k)$ denote the information transmitted on the kth subcarrier of the lth OFDM symbol. Furthermore, let $\boldsymbol{x}_l = [x_l(0), \ldots, x_l(\bar{N}-1)]^T$ denote the $\bar{N} \times 1$ vector containing the lth frequency-domain OFDM symbol where $(\cdot)^T$ denotes the vector transpose operation. The transmitted frequency-domain OFDM symbol corresponding to the PSS with root index r is given by $[0, \mathrm{P}_r^{63}(32), \ldots, \mathrm{P}_r^{63}(62), \mathbf{0}_{\bar{N}-63}^T, \mathrm{P}_r^{63}(0), \ldots, \mathrm{P}_r^{63}(30)]^T$ where $\mathbf{0}_k$ denotes the $k \times 1$ vector whose entries are all equal to 0. Note that PSS transmission is performed using 62 sub-carriers in total; with 31 sub-carriers mapped on each side of the dc sub-carrier. In addition, $\mathrm{P}_r^{63}(31)$ is not used to avoid modulating the dc subcarrier.

The SSS is transmitted on the same subcarriers used for PSS transmission. The SSS is constructed by interleaving, in the frequency domain, two length-31 BPSK-modulated sequences. The two sequences defining the SSS differ between subframe 0 and subframe 5 to enable the UE to identify the frame boundary. Each of the two frequency-domain SSS sequences is constructed by scrambling and cyclic shifting of a basic maximum length sequence (m-sequence). The scrambling codes are also constructed from cyclic-shifted m-sequences [24]. The scrambling codes and the cyclic shifts depend on the physical-layer identity, $N_{\mathrm{ID}}^{(2)}$, as well as the physical-layer cell identity group, termed $N_{\mathrm{ID}}^{(1)}$, which is an integer between 0 and 167. The physical-layer cell identity is defined as

$$N_{\mathrm{ID}} = 3N_{\mathrm{ID}}^{(1)} + N_{\mathrm{ID}}^{(2)}, \tag{2}$$

and is an integer between 0 and 503.

The lth OFDM symbol is generated by performing an $\bar{N}$-point inverse discrete Fourier transform (IDFT) on the information symbols $\{x_l(k)\}_{k=0}^{\bar{N}-1}$ and inserting CP samples before the IDFT output. The OFDM symbol is transmitted over a carrier through the channel which is assumed to be block stationary, i.e., time-invariant during each

OFDM symbol. At the UE, the received passband signal is down converted to baseband. Let Δf denote the mismatch between the carrier frequency of the transmitter and the receiver. We can write the $\bar{N} \times 1$ received signal vector–after CP removal–corresponding to the transmission of the lth OFDM symbol as

$$\bar{\boldsymbol{y}}_l = \bar{\boldsymbol{E}}_l \bar{\boldsymbol{F}} \boldsymbol{H}_l \boldsymbol{x}_l + \bar{\boldsymbol{n}}_l \tag{3}$$

where $\boldsymbol{H}_l = \mathrm{diag}\{H_l(0), H_l(1), \ldots, H_l(\bar{N}-1)\}$ is a diagonal matrix containing the frequency response of the channel during the transmission of the lth OFDM symbol, $\bar{\boldsymbol{F}}$ is the $\bar{N} \times \bar{N}$ IDFT matrix whose (n, k)th element is given by $\frac{1}{\sqrt{\bar{N}}} e^{j\frac{2\pi nk}{\bar{N}}}$ for $n, k = 0, \ldots, \bar{N}-1$, and the $\bar{N} \times \bar{N}$ diagonal matrix $\bar{\boldsymbol{E}}_l$ is given by[1]

$$\bar{\boldsymbol{E}}_l = e^{j\frac{2\pi \Delta f (l-1)(\bar{N}+\bar{N}_g)}{\bar{f}_s}} \mathrm{diag}\left\{1, e^{j\frac{2\pi \Delta f}{\bar{f}_s}}, \ldots, e^{j\frac{j2\pi(\bar{N}-1)\Delta f}{\bar{f}_s}}\right\} \tag{4}$$

where $\bar{N}_g$ is the CP length. In (3), the $\bar{N} \times 1$ vector $\bar{\boldsymbol{n}}_l$ contains the samples of the interference-plus-noise received with the lth OFDM symbol whose elements are independent of the transmitted information symbols.

Classical LTE synchronization algorithms start with PSS detection and decoding and proceed to SSS detection only after successful identification of the PSS sequence. Joint PSS detection and identification algorithms can operate on the received time-domain or frequency-domain samples. Time-domain algorithms search for the peak of the cross-correlation between the received samples and the three PSS signature sequences, e.g., [25]–[28]. Reduced complexity algorithms that decouple PSS detection and identification were also proposed. These algorithms exploit the central symmetry of the PSS or cross-correlate the received signal with the sum of the three PSS signature sequences [18], [29].

Frequency domain PSS detection and decoding algorithms consist of two stages. First, coarse synchronisation is done to locate the boundaries of the OFDM symbols using the CP-based correlation method. Afterwards, PSS localization and identification can also be performed in the frequency-domain by computing the cross-correlation between the discrete Fourier transform (DFT) of the detected PSS vector and the ZC sequences [30]. The cross-correlation is computed using the 62 subcarriers corresponding to the active PSS subcarriers. However, in the presence of strong interference, the performance of CP-based correlation based methods severely deteriorates which renders frequency-domain PSS detection methods ineffective. In order to illustrate the effect of interference on CP-based correlation methods, the downlink of an FDD LTE system with 1.25 MHz BW and extended mode CP is simulated. We consider an interference signal occupying the band from 300 KHz to 390 KHz, i.e., the interference signal occupies approximately 10% of the bandwidth of the PSS signal. Fig. 2 shows the probability of detecting the boundary of the OFDM signal with an error less than 5 samples versus the signal-to-noise ratio in the absence and presence of interference. We can see from Fig. 2 that even when the ISR is as low as 0 dB, the performance of CP-based methods severely deteriorates compared to the case when the interference is absent.

[1]The expression in (4) is valid only for the extended CP mode where all the OFDM symbols have the same CP length.

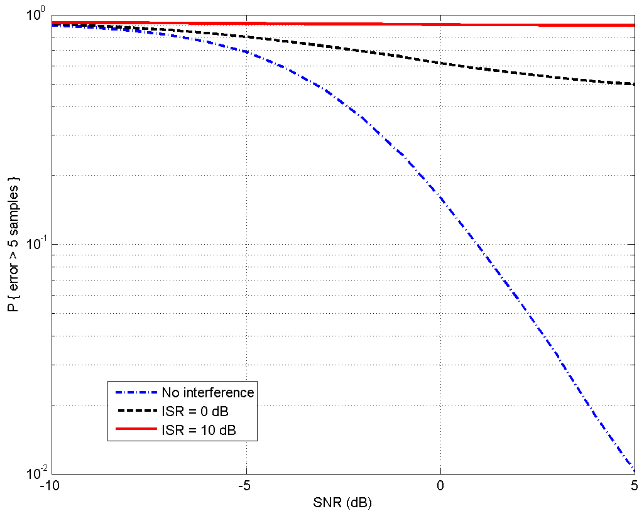

FIGURE 2. Probability of error in finding the location of the OFDM symbol with at least five samples accuracy.

After PSS detection and decoding, classical LTE synchronization algorithms proceed to SSS detection and decoding [24]. Since the CP and duplexing modes are still unknown, the receiver has to detect the location of the SSS sequence at all possible positions, e.g., via exploiting the conjugate symmetry of SSS waveform in the time-domain [29]. Afterwards, the receiver decodes the SSS either coherently or incoherently. In the case of coherent detection, the UE obtains the channel estimate from the detected PSS [31].

III. ADAPTIVE SYNCHRONIZATION ALGORITHM

In this section, we present a novel synchronization algorithm for LTE systems with improved robustness against partial-band interference. The objective of the synchronization algorithm is to estimate the frame timing, CFO, physical-layer cell identity, CP length, and duplexing mode. This is accomplished by locating the PSS and SSS within the LTE downlink frame and decoding the information contained in them. The physical-layer identity and slot timing can be obtained from PSS processing while the physical-layer cell identity group, CP length, duplexing mode, and frame timing are obtained from SSS processing. After locating the PSS and SSS, the proposed algorithm estimates the CFO using the information contained in the received synchronization signals. The proposed algorithm can be divided into the following three parts; PSS detection and processing, SSS detection and processing, and CFO estimation.

A. PSS DETECTION AND PROCESSING

Fig. 3 shows a block diagram of the proposed PSS processing algorithm. The algorithm receives a time-domain

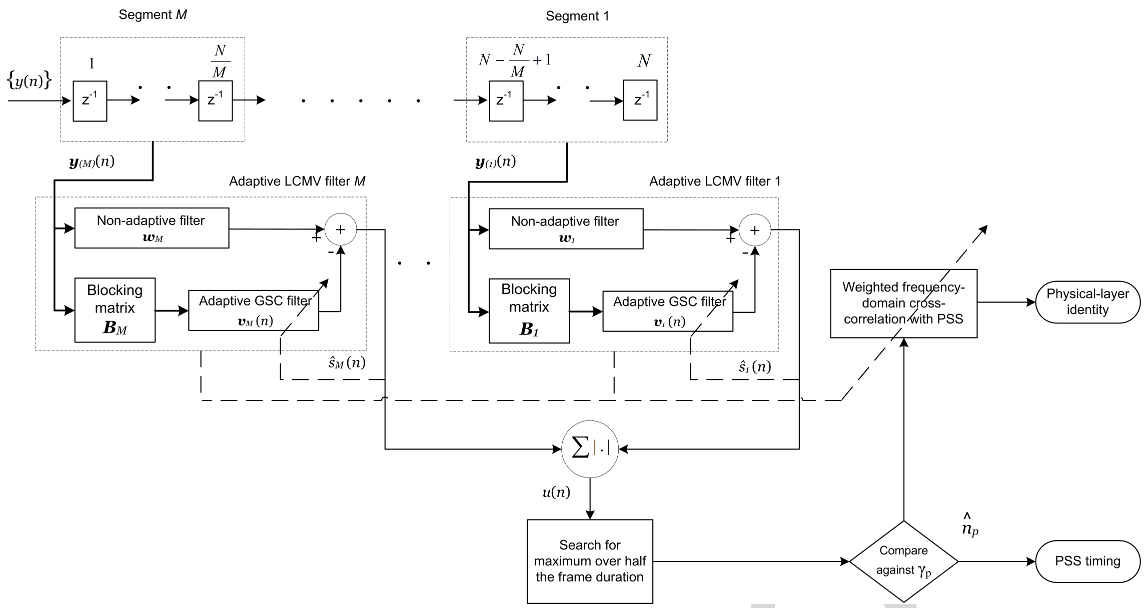

FIGURE 3. **Block diagram of the proposed adaptive detection algorithm.**

low-pass filtered baseband signal of BW 480 KHz sampled at $f_s \geq 960$ KHz. Since the duration of one OFDM symbol–without the CP–is given by $T = 66.67\mu$s, the number of samples corresponding to one OFDM symbol is given by $N = f_s T$, i.e., at $f_s = 960$ KHz, $N = 64$. Recall that the synchronization signals are located on the 62 central subcarriers around the dc subcarrier, and hence, the low-pass filtered input samples contain all the transmitted information in the LTE downlink synchronization signals. It is worth mentioning that increasing the sampling rate beyond 960 KHz provides an oversampling gain at the cost of increasing the computational complexity of the proposed algorithm [32].

The PSS processing algorithm can be divided into two main stages. In the first one, M parallel adaptive LCMV filters are used to suppress the output corresponding to the received signal vectors that do not correspond to PSS transmission. The algorithm utilizes the outputs of these adaptive filters to detect the location of the PSS signal within the received LTE downlink signal. In the second stage, the physical-layer identity is estimated by finding the ZC sequence that has the highest "weighted" cross-correlation with the detected PSS sequence in the frequency-domain.

1) ADAPTIVE FILTERING AND PSS LOCALIZATION

Let $y(n)$ denote the nth sample of the input time-domain low-pass filtered signal. Furthermore, let $\boldsymbol{y}(n) = [y(n), \ldots, y(n + N - 1)]^T$ represent the $N \times 1$ vector containing the latest N samples of $\{y(n)\}$ at time instant $n + N - 1$. The vector $\boldsymbol{y}(n)$ is divided into M segments, $\{\boldsymbol{y}_{(m)}(n)\}_{m=1}^{M}$, each of length $\frac{N}{M}$ where

$$\boldsymbol{y}_{(m)}(n) = \left[y\left(n + (m-1)\frac{N}{M}\right), \ldots, y\left(n + \frac{mN}{M} - 1\right)\right]^T. \tag{5}$$

The mth segment of the vector $\boldsymbol{y}(n)$ is linearly processed by the adaptive filter, $\boldsymbol{g}_{(m)}(n)$, to produce the filtered output $s_{(m)}(n)$ which is given by

$$s_{(m)}(n) = \boldsymbol{g}_{(m)}^H(n)\boldsymbol{y}_{(m)}(n) \tag{6}$$

where $(\cdot)^H$ denotes the Hermitian transpose operator and $\boldsymbol{g}_{(m)}(n) = [g_{(m),0}(n), \ldots, g_{(m),\frac{N}{M}-1}(n)]^T$ is the $\frac{N}{M} \times 1$ vector containing the coefficients of the adaptive filter at the nth time instant.

We design the coefficients of the adaptive filters using the LCMV design criterion, i.e., we minimize the output power of each filter while preserving the outputs corresponding to the transmission of any of the three possible PSS signatures. Let the $N \times 1$ vector $\boldsymbol{c}_i$ represent the input received signal vector corresponding to transmission of the PSS with $N_{\mathrm{ID}}^{(2)} = i$, where $i = 0$, 1, and 2. Furthermore, let $\boldsymbol{c}_{(m),i}$ denote the mth segment of the vector $\boldsymbol{c}_i$. Therefore, the vector $\boldsymbol{g}_{(m)}(n)$ can be obtained by solving the following optimization problem

$$\min_{\boldsymbol{g}_{(m)}(n)} \; \boldsymbol{g}_{(m)}^H(n)\boldsymbol{R}_{(m)}(n)\boldsymbol{g}_{(m)}(n)$$

$$\text{subject to } \; \boldsymbol{g}_{(m)}^H(n)\boldsymbol{c}_{(m),i} = \frac{1}{M} \quad \text{for } i = 0, 1, 2 \tag{7}$$

where $\boldsymbol{R}_{(m)}(n) = \mathrm{E}\{\boldsymbol{y}_{(m)}(n)\boldsymbol{y}_{(m)}^H(n)\}$ is the covariance matrix of $\boldsymbol{y}_{(m)}(n)$, and $\mathrm{E}\{\cdot\}$ denotes the statistical expectation.

The above LCMV optimization problem can be converted to an equivalent unconstrained optimization problem by using the GSC decomposition of the adaptive filter coefficients [33]. In particular, let us define the $\frac{N}{M} \times 3$ matrix $\boldsymbol{C}_{(m)}$ whose columns contain the mth segment of all possible three PSS signatures, i.e., $\boldsymbol{C}_{(m)} = [\boldsymbol{c}_{(m),0}, \boldsymbol{c}_{(m),1}, \boldsymbol{c}_{(m),2}]$. Let $\boldsymbol{B}_{(m)}$ denote the $\frac{N}{M} \times (\frac{N}{M} - 3)$ matrix whose columns span the nullspace of $\boldsymbol{C}_{(m)}^H$, i.e., $\boldsymbol{B}_{(m)}^H\boldsymbol{c}_{(m),i} = \boldsymbol{0}_{\frac{N}{M}-3}$ for $i = 0$, 1, and 2.

Using the matrix $\boldsymbol{B}_{(m)}$, we can decompose the vector $\boldsymbol{g}_{(m)}(n)$ into

$$\boldsymbol{g}_{(m)}(n) = \boldsymbol{w}_{(m)} - \boldsymbol{B}_{(m)}\boldsymbol{v}_{(m)}(n) \tag{8}$$

where

$$\boldsymbol{w}_{(m)} = \frac{1}{M}\boldsymbol{C}_{(m)}\left(\boldsymbol{C}_{(m)}^{H}\boldsymbol{C}_{(m)}\right)^{-1}\mathbf{1}_3 \tag{9}$$

is a fixed weight vector, i.e., independent of n, $\mathbf{1}_k$ is the $k\times 1$ vector whose entries are all equal to 1, and the $(\frac{N}{M}-3)\times 1$ vector $\boldsymbol{v}_{(m)}(n)$ contains the adaptive GSC filter coefficients at time instant n. By substituting with (8) in (7), we can convert the LCMV problem into the following unconstrained optimization problem

$$\min_{\boldsymbol{v}_{(m)}(n)} \left(\boldsymbol{w}_{(m)} - \boldsymbol{B}_{(m)}\boldsymbol{v}_{(m)}(n)\right)^{H}\boldsymbol{R}_{(m)}(n)\left(\boldsymbol{w}_{(m)} - \boldsymbol{B}_{(m)}\boldsymbol{v}_{(m)}(n)\right) \tag{10}$$

where the adaptive GSC weight vector that yields the optimal solution of (10) is given by

$$\boldsymbol{v}^{\star}_{(m)}(n) = \left(\boldsymbol{B}_{(m)}^{H}\boldsymbol{R}_{(m)}(n)\boldsymbol{B}_{(m)}\right)^{-1}\boldsymbol{B}_{(m)}^{H}\boldsymbol{R}_{(m)}(n)\boldsymbol{w}_{(m)}. \tag{11}$$

Since the covariance matrix $\boldsymbol{R}_{(m)}(n)$ is not readily available at the receiver, we employ the RLS algorithm to estimate the adaptive GSC weight vector iteratively from the received signal samples. The RLS algorithm is initialized by setting the initial weight vector estimate as $\hat{\boldsymbol{v}}_{(m)}(0) = \mathbf{0}_{\frac{N}{M}-3}$ and its associated covariance matrix as $\boldsymbol{P}_{(m)}(0) = \delta\boldsymbol{I}_{\frac{N}{M}-3}$ where $\boldsymbol{I}_k$ denotes the $k\times k$ identity matrix and δ is a large number, e.g., $\delta = 10$. Given the estimate of the filter coefficients at time instant $n-1$, $\hat{\boldsymbol{v}}_{(m)}(n-1)$, and its associated covariance $\boldsymbol{P}_{(m)}(n-1)$, the RLS algorithm computes the gain vector $\boldsymbol{k}_{(m)}(n)$ as

$$\boldsymbol{k}_{(m)}(n) = \frac{\boldsymbol{P}_{(m)}(n-1)\boldsymbol{B}_{(m)}^{H}\boldsymbol{y}_{(m)}(n)}{\lambda + \boldsymbol{y}_{(m)}^{H}(n)\boldsymbol{B}_{(m)}\boldsymbol{P}_{(m)}(n-1)\boldsymbol{B}_{(m)}^{H}\boldsymbol{y}_{(m)}(n)}. \tag{12}$$

where λ is the RLS forgetting factor that gives exponentially less weight to older samples. The filter coefficients and the associated covariance are updated respectively by

$$\hat{\boldsymbol{v}}_{(m)}(n) = \hat{\boldsymbol{v}}_{(m)}(n-1) + \boldsymbol{k}_{(m)}(n)\hat{s}^{*}_{(m)}(n) \tag{13}$$

$$\boldsymbol{P}_{(m)}(n) = \frac{1}{\lambda}\left(\boldsymbol{P}_{(m)}(n-1) - \boldsymbol{k}_{(m)}(n)\boldsymbol{y}_{(m)}^{H}(n)\boldsymbol{B}_{(m)}\boldsymbol{P}_{(m)}(n-1)\right) \tag{14}$$

where $(\cdot)^{*}$ denotes the complex conjugate operator and $\hat{s}_{(m)}(n)$ is the output of the mth LCMV filter at the nth time instant computed using the estimate of the optimal GSC filter coefficients at time instant $n-1$, i.e.,

$$\hat{s}_{(m)}(n) = \boldsymbol{w}_{(m)}^{H}\boldsymbol{y}_{(m)}(n) - \hat{\boldsymbol{v}}_{(m)}^{H}(n-1)\boldsymbol{B}_{(m)}^{H}\boldsymbol{y}_{(m)}(n). \tag{15}$$

Note that $\hat{s}_{(m)}(n)$ is an estimate of the ideal filter output $s_{(m)}(n)$ in (6) as it is calculated using the weight vector estimate at time $n-1$ instead of the optimum weight vector at time n.

The outputs of the M filters are combined to yield the PSS-detection metric $u(n)$ which is given by

$$u(n) = \sum_{m=1}^{M}\left|\hat{s}_{(m)}(n)\right| \tag{16}$$

where $|\cdot|$ denotes the magnitude of a complex number. Due to utilizing the LCMV design criterion, each LCMV filter will suppress its output except when the input corresponds to one of the three possible PSS signatures. As a result, the metric $u(n)$ can be utilized to search for the location of the PSS signal within the downlink frame. The PSS detection algorithm locates the PSS by searching for the sample index that corresponds to the maximum value of $u(n)$ over half the frame duration, i.e., the search is performed over $5\times 10^{-3}f_s$ samples. Let $\hat{n}_P$ denote the samples index corresponding to the maximum value of $u(n)$ over the search window. The proposed algorithm declares detection of the PSS signal at $n = \hat{n}_P$ if

$$\left|u(\hat{n}_P)\right| \geq \gamma_p \tag{17}$$

where γ_p is a predetermined threshold that can be used to control the probabilities of detection and false alarm.

Remark 1: The number of complex multiplication operations required to implement (12)–(15) is $\frac{3N^2}{M^2} - \frac{13N}{M} + 12$ operations.[2] Since the number of adaptive filters is given by M, the computational complexity of the adaptive filtering module of the proposed algorithm is of $\mathcal{O}\{\frac{N^2}{M}\}$. Increasing the number of segments M reduces the computational complexity of the algorithm.

Remark 2: Since the length of each adaptive filter is given by $\frac{N}{M}$ and the number of linear constraints in (7) is 3, each adaptive filter can effectively suppress the interference signal as long as the rank of the interference covariance matrix does not exceed $\frac{N}{M}-3$. Increasing the number of segments M leads to decreasing the interference rejection capability of the proposed algorithm. This will be illustrated via numerical simulations in Section IV.

Remark 3: In the presence of a CFO of magnitude Δf, the phase deviation over the length of the PSS signature $\boldsymbol{c}_{(m),i}$ is given by $\frac{2\pi(N-M)\Delta f}{Mf_s}$. Increasing the number of segments M leads to decreasing the phase deviation due to CFO. As a result, for a given CFO, the distance between the received PSS signal and the subspace containing the protected PSS signatures decreases as the number of segments increases. Therefore, increasing the number of segments improves the robustness of the algorithm towards CFO mismatches. A detailed analysis of the effect of the number of segments on the PSS detection metric is presented in the Appendix.

[2] This expression was calculated by assuming that the vectors $\boldsymbol{B}_{(m)}^{H}\boldsymbol{y}_{(m)}(n)$ and $\boldsymbol{P}_{(m)}(n-1)\boldsymbol{B}_{(m)}^{H}\boldsymbol{y}_{(m)}(n)$ are calculated first and stored. Hence, the number of multiplication operations required to calculate the filter gain in (12) is given by $\frac{2N^2}{M^2} - \frac{8N}{M} + 6$ and the number of multiplication operations required to compute (13) and (14) is given by $\frac{N}{M} - 3$ and $(\frac{N}{M} - 3)^2$, respectively.

2) PHYSICAL-LAYER IDENTITY ESTIMATION

Since the LCMV filtering algorithm is designed to have the same output for all possible PSS signatures, the physical-layer identity cannot be directly determined from the metric $u(n)$. Note that due to utilizing the LCMV design criteria, the adaptive filters minimize the output resulting from the contribution of the interference signal at the PSS detection instant. As a result, the frequency response of the filters at the detection instant provides information about the power spectral density of the interference signal. Let $\boldsymbol{Y}_P = [Y_P(0), \ldots, Y_P(N-1)]^T$ denote the N-point DFT of the received vector $\boldsymbol{y}(\hat{n}_P)$ at the PSS-detection instant. Also, let the $N \times 1$ vector $\boldsymbol{g}$ denote the concatenation of the adaptive LCMV filters corresponding to the M segments at the PSS detection instant, i.e.,

$$\boldsymbol{g} = \left[\boldsymbol{w}_{(1)}^T - \hat{\boldsymbol{v}}_{(1)}^T(\hat{n}_P)\boldsymbol{B}_{(1)}^T, \ldots, \boldsymbol{w}_{(M)}^T - \hat{\boldsymbol{v}}_{(M)}^T(\hat{n}_P)\boldsymbol{B}_{(M)}^T\right]^T. \quad (18)$$

Furthermore, let $\boldsymbol{G} = [G(0), \ldots G(N-1)]^T$ represent the N-point DFT of $\boldsymbol{g}^*$. Therefore, the frequency response of the concatenated LCMV filter at the detection instant can be used to suppress the interference signal. The received PSS symbol on the kth subcarrier after interference suppression is computed as

$$V(k) = Y_P(k)G(-k). \quad (19)$$

The physical-layer identity can be estimated by computing the cross-correlation in the frequency domain between the interference-free received signal and the three PSS signature vectors. However, the PSS signature vectors $\boldsymbol{c}_i$ should be modified to account for the effect of the interference suppression operation in (19). Let $c_{i,l}$ represent the lth component of the signature vector $\boldsymbol{c}_i$ of the PSS transmission corresponding to physical-layer identity i, i.e., $\boldsymbol{c}_i = [c_{i,0}, \ldots c_{i,N-1}]^T$. Let $\boldsymbol{C}_i = [C_i(0), \ldots, C_i(N-1)]^T$ denote the N-point DFT of $\boldsymbol{c}_i$. The filtered frequency-domain signature sequence of the PSS transmission corresponding to physical-layer identity i is computed as

$$\tilde{C}_i(k) = C_i(k)G(-k). \quad (20)$$

Using (19) and (20), the physical-layer identity is estimated as

$$\hat{N}_{\mathrm{ID}}^{(2)} = \arg\max_{i=0,1,2} \left|\sum_{k=0}^{N-1} V^*(k)\tilde{C}_i(k)\right| \quad (21)$$

$$= \arg\max_{i=0,1,2} \left|\sum_{k=0}^{N-1} |G(-k)|^2 Y_P^*(k)C_i(k)\right|. \quad (22)$$

The expression in (22) is a weighted frequency-domain cross-correlation of the detected PSS signal with candidate PSS sequences. The weighting is done using the squared magnitude response of the concatenated LCMV filter at the detection instant in order to eliminate the contribution of the interference signal to the computed cross-correlation metric in (22).

B. SSS DETECTION AND PROCESSING

After detecting the physical-layer identity, the CP type and the duplexing mode can be detected together with the physical-layer cell identity group. The detection is performed via weighted frequency-domain cross-correlation of all possible 168 SSS signature waveforms with the received signal at the 4 candidate locations of the SSS sequence. We assume that the power spectral density of the interference signal does not change significantly over the temporal duration between SSS and PSS transmission. Hence, the cross-correlation weighting is done using the frequency response of the LCMV filter at the detection instant of the PSS.

Given the sampling rate of the algorithm, f_s, and the PSS timing, $\hat{n}_P$, there are 4 possible locations of the SSS which are given by leftmargin=*

1) $n_{S,1} = \hat{n}_P - N - T_N f_s$: for FDD with normal CP mode
2) $n_{S,2} = \hat{n}_P - N - T_E f_s$: for FDD with extended CP mode
3) $n_{S,3} = \hat{n}_P - 3N - 3T_N f_s$: for TDD with normal CP mode
4) $n_{S,4} = \hat{n}_P - 3N - 3T_E f_s$: for TDD with extended CP mode

where $T_N = 4.69 \times 10^{-6}$ and $T_E = 16.67 \times 10^{-6}$ are the durations of the CP of one OFDM symbol in the normal CP and extended CP modes, respectively. Let the $N \times 1$ vector $\boldsymbol{y}_{n_{S,i}} = \left[y\left(n_{S,i}\right), y\left(n_{S,i}+1\right) \ldots, y\left(n_{S,i}+N-1\right)\right]^T$ where $i = 1, \ldots, 4$ represent the ith candidate received SSS vector. Furthermore, let $\boldsymbol{s}_j = [s_{j,0}, \ldots s_{j,N-1}]^T$ denote the SSS signature vector corresponding to physical-layer cell identity group $N_{\mathrm{ID}}^{(1)} = j$ associated with the estimated physical-layer identity $\hat{N}_{\mathrm{ID}}^{(2)}$. Similar to physical-layer identity estimation algorithm in Subsection III-A.2, the location of the SSS and the physical-layer cell identity group can be jointly estimated via weighted frequency-domain cross correlation as

$$\left\{\hat{N}_{\mathrm{ID}}^{(1)}, \hat{n}_S\right\} = \arg\max_{j=0,\ldots,167, i=1,\ldots,4} \left|\sum_{k=0}^{N-1} |G(-k)|^2 Y_{S,i}^*(k)S_j(k)\right| \quad (23)$$

where $Y_{S,i}(k)$ and $S_j(k)$ are given respectively by

$$Y_{S,i}(k) = \frac{1}{\sqrt{N}} \sum_{n=0}^{N-1} y(n_{S,i}+n)e^{-j\frac{2\pi nk}{N}}, \quad (24)$$

$$S_j(k) = \frac{1}{\sqrt{N}} \sum_{n=0}^{N-1} s_{j,n}e^{-j\frac{2\pi nk}{N}}. \quad (25)$$

Note that we have utilized the frequency response of the adaptive LCMV filter at the PSS detection instant to suppress the contribution of the interference signal to the cross-correlation metric in (23). Since $S_j(k) \in \{0, 1, -1\}$ for all k, j, the number of multiplications required to compute the cross correlation metrics in (23) is only $8N$ real-valued multiplications.

C. CARRIER FREQUENCY OFFSET ESTIMATION

After locating and decoding the received PSS and SSS, the CFO can be estimated by joint processing of the DFT of the received PSS and SSS in the frequency domain. The proposed algorithm exploits the CFO-induced phase shift between the samples of the received PSS and the SSS to estimate the CFO [34]. The magnitude response of the adaptive LCMV filter at the detection instant is also utilized to reduce the effect of the interference signal on the CFO estimate. We can write the DFT of the lth received time-domain OFDM symbol–given by (3)–at the kth subcarrier as [34]

$$\bar{Y}_l(k) = e^{j\frac{\pi\Delta f(\bar{N}-1)}{\bar{f}_s}+\theta_l}\frac{\sin(\frac{\pi\bar{N}\Delta f}{\bar{f}_s})}{\bar{N}\sin(\frac{\pi\Delta f}{\bar{f}_s})}H_l(k)x_l(k)+\bar{I}_{l,k}+\bar{N}_{l,k} \tag{26}$$

where

$$\theta_l = \frac{2\pi\Delta f(l-1)(\bar{N}+\bar{N}_g)}{\bar{f}_s} \tag{27}$$

is the component of the CFO-induced phase shift that depends on the location of the OFDM symbol within the downlink frame. The first term in (26) is the transmitted information symbol on the kth subcarrier multiplied by the corresponding frequency response of the channel. This component experiences an amplitude reduction and phase shift due to CFO. The second term in (26) is the inter-carrier interference caused by CFO while the third term is the interference-plus-noise at the kth subcarrier.

The proposed CFO estimation algorithm exploits the phase shift induced by CFO that depends on the location of the OFDM symbol in the frame, and the frame timing information obtained from PSS and SSS detection, i.e., the difference between $\hat{n}_P$ and $\hat{n}_S$. We utilize the frequency response of the adaptive LCMV filter at the PSS detection instant to reduce the effect of the interference signal on the CFO estimation metric. The CFO estimation metric $\hat{\theta}$ is computed as

$$\hat{\theta} = \angle\left\{\sum_{k=0}^{N-1}|G(-k)|^2Y_P(k)C^*_{\hat{N}^{(2)}_{\mathrm{ID}}}(k)\left(|G(-k)|^2Y_S(k)S^*_{\hat{N}^{(1)}_{\mathrm{ID}}}(k)\right)^*\right\} \tag{28}$$

where $\angle\{z\}$ denotes the phase of the complex number z and $Y_S(k)$ is the DFT of the detected SSS sequence at the kth subcarrier. Assuming that the frequency response of the channel is constant over the temporal window spanning the duration of PSS and SSS transmission, and neglecting the inter-carrier interference and the interference-plus-noise terms in (26), we can estimate the CFO as

$$\Delta\hat{f} = \frac{f_s\hat{\theta}}{2\pi(\hat{n}_P-\hat{n}_S)}. \tag{29}$$

Note that the proposed CFO estimation algorithm has a limited range of detection that depends on the temporal separation between the PSS and SSS. In particular, the maximum CFO value that can be detected is given by ± 7 KHz in the case of FDD with normal CP, and ± 2 KHz in the case of TDD with extended CP mode.[3]

IV. NUMERICAL SIMULATIONS

In this section, the performance of the proposed adaptive synchronization algorithm is evaluated using numerical simulations. The downlink of an FDD LTE system with 1.25 MHz BW and normal mode CP is simulated. The sampling frequency for the adaptive algorithm is set to $f_s = 960$ KHz resulting in a processing window of length $N = 64$ samples. Simulation results are obtained by averaging over 400 Monte Carlo runs. In each run, the cell identity is generated randomly. The synchronization algorithm is considered successful if the detected cell identity, CP mode, and duplexing mode match the true values of the system as well as the estimate of the frame start index is within the length of the CP of the first OFDM symbol. A false alarm event is declared when any of the above conditions is violated given that the threshold $\gamma_p = 0.3$ is crossed during PSS search. The parameters of the adaptive GSC filter are selected as $\lambda = 0.98$ for $M = 1$ and $\lambda = 0.95$ for $M = 2$ while the RLS covariance initialization parameter δ was selected as $\delta = 10$.

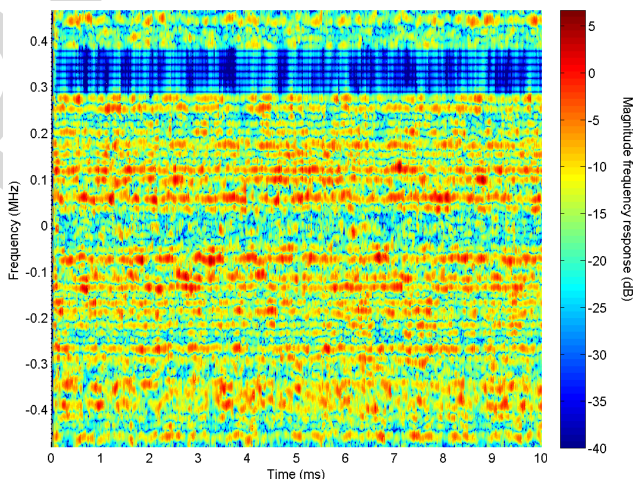

FIGURE 4. Frequency response of the adaptive LCMV filter over the duration of one LTE frame (partial band interference scenario).

Similar to [36]–[39], we consider an interference signal composed of a superposition of modulated sinusoids. Unless stated otherwise, the interference signal is generated as a collection of seven single tones with 15 KHz spacing occupying the band from 300 KHz to 390 KHz. The interference signal is held active over the entire frame duration. In order to focus on illustrating the performance of the PSS detection algorithm, first, a frequency-nonselective channel is considered. The ISR is set to 20 dB. Fig. 4 shows the magnitude response of the proposed adaptive LCMV filtering algorithm with $M = 1$

[3]The detection range of the algorithm can be extended by adding an integer CFO estimation stage together with the PSS localization algorithm in Section III-A.2. For example, multiple parallel adaptive filters can be used to detect the PSS location and the integer CFO where each filter is designed to preserve the integer CFO-modulated PSS signatures [35].

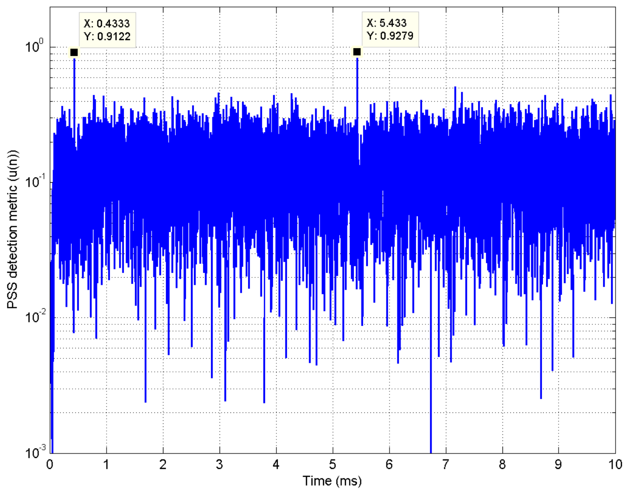

FIGURE 5. Magnitude of the adaptive LCMV filter output versus time.

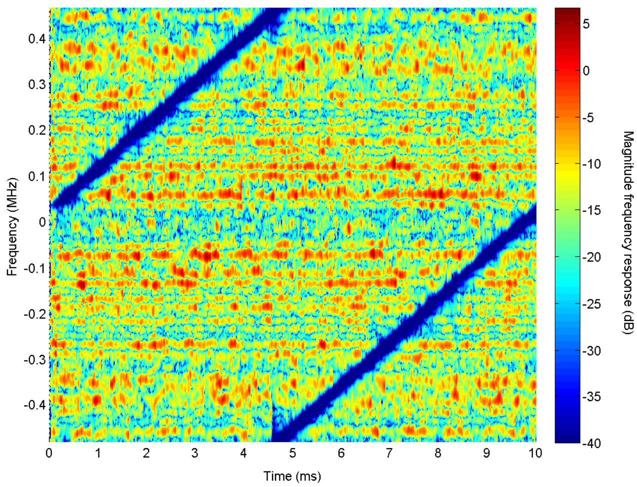

FIGURE 6. Frequency response of the adaptive LCMV filter over the duration of one LTE frame (chirp jamming scenario).

over the temporal duration of one LTE frame. We can see from this figure that the LCMV filter places deep nulls at the frequencies of the interference signal over the whole temporal duration of the interference signal. As a result, the interference signal is effectively blocked from the output of the adaptive filter. Fig. 5 shows the PSS detection metric, $u(n)$, versus time over the duration of one frame. It can be seen from this figure that the metric has two peaks that are spaced 5 ms apart corresponding to the locations of the PSS within one LTE frame. Fig. 5 also shows that the adaptive filter can effectively remove the contribution of the interference signal where the peak-to-side-peak ratio is around 2.

In order to illustrate the ability of the proposed synchronization algorithm to rapidly adapt to the jamming signal, we consider a jamming signal whose frequency chirps linearly from -480 KHz to 480 KHz in a time interval of duration 10 ms. The jamming signal is present over the entire frame duration and the jamming-to-signal (JSR) ratio is set to 20 dB. The parameters of the algorithm are selected as $M = 1$, $\lambda = 0.98$, and $\delta = 10$. In order to focus on illustrating the performance of the PSS detection algorithm, we also consider a frequency-nonselective channel. Fig. 6 shows the magnitude response of the adaptive LCMV filter over the temporal duration of one LTE frame. We can see from this figure that the proposed algorithm can effectively track the jamming signal by placing deep nulls at its spectral components. The PSS detection metric also showed two clear peaks that are spaced 5 ms apart similar to those observed in Fig. 5.

Next, we compare the performance of the proposed algorithm to that of a classical non-robust LTE synchronization algorithm that employs time-domain cross-correlation with the stored PSS signature waveforms to detect the PSS location and estimate the physical-layer identity. The non-robust synchronization algorithm then searches for the SSS and decodes it by using time-domain cross-correlation with all possible SSS signature waveforms. The non-robust synchronization algorithm is implemented at a sampling frequency equal to 1.92 MHz which corresponds to the system BW, i.e., twice the sampling frequency of the proposed adaptive algorithm.

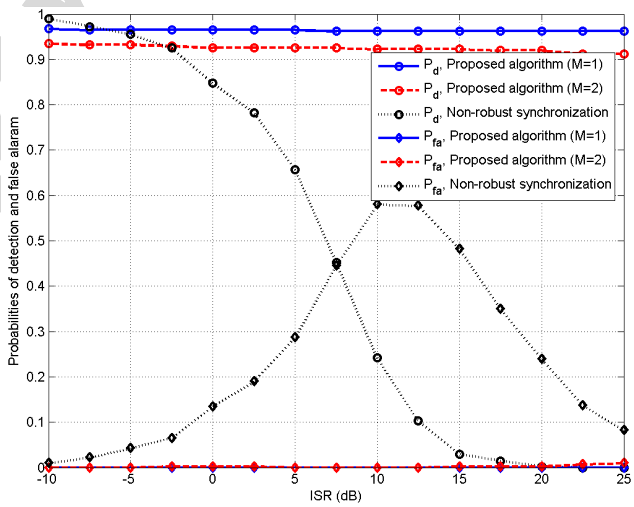

FIGURE 7. Probabilities of detection and false alarm versus ISR.

Fig. 7 shows the probabilities of detection and false alarm versus ISR for the Extended Pedestrian A channel model with 5 Hz Doppler (EPA5). As seen from this figure, the proposed algorithm maintains a high probability of detection and a probability of false alarm almost equal to zero for all tested ISR values. In contrast, the performance of the non-robust synchronization algorithm starts to deteriorate when the ISR increases above 0 dB. In fact, the probability of correct detection is almost zero when the ISR is 20 dB. Furthermore, there is a non-zero probability of false alarm caused by the correlation peaks generated due to interference leakage. In contrast, the constraints in the proposed LCMV adaptive filtering algorithm ensure a distortion-less response to the received PSS signal while effectively removing the interference signal. We can also notice that increasing the number of segments from $M = 1$ to $M = 2$ slightly reduces the probability of detection due to decreasing the interference cancellation capability of the algorithm. However, as mentioned in Section III, increasing the number of segments reduces the computational complexity of the algorithm and increases its robustness against PSS signature mismatches.

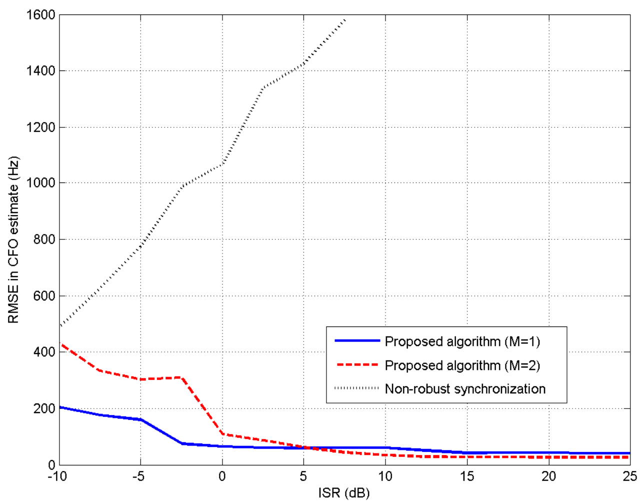

FIGURE 8. RMSE in CFO estimate versus ISR.

Fig. 8 shows the root mean square error (RMSE) in CFO estimate versus ISR for different algorithms. The RMSE is computed only when the probability of detection is higher than 0.25 by averaging only over the runs in which correct detection occurred. As seen from this figure, the accuracy of the CFO estimates produced by the non-robust algorithm deteriorate rapidly as the ISR increases. In contrast, the proposed algorithm can produce a very accurate estimate of the CFO. In fact the accuracy of the CFO estimate of the proposed algorithm is better at high ISR than at low and intermediate values. This can be attributed to the fact that at high ISR, the LCMV filter places deep nulls at the interference frequencies which effectively eliminates the contribution of the interference signal to the CFO estimation metric in (28).

In order to investigate the effect of the interference signal BW on the performance of the proposed algorithm, interference signals of various BW are created as sums of single tones with 15 KHz spacing starting from $f_{\min}$ to $f_{\max} = 390$ KHz. We define the relative BW of the interference signal as

$$\mathrm{BW_r} \triangleq \frac{f_{\max} - f_{\min}}{62 \times 15 \times 10^3} \tag{30}$$

which represents the fraction of PSS and SSS subcarriers affected by interference. Fig. 9 and Fig. 10 show the probabilities of detection and false alarm versus the relative BW of the interference signal at two ISR values. We can see from these figures that the proposed synchronization algorithm with $M = 1$ can effectively combat the interference signal even when it covers one third of the BW of the synchronization signals. When the interference power is distributed

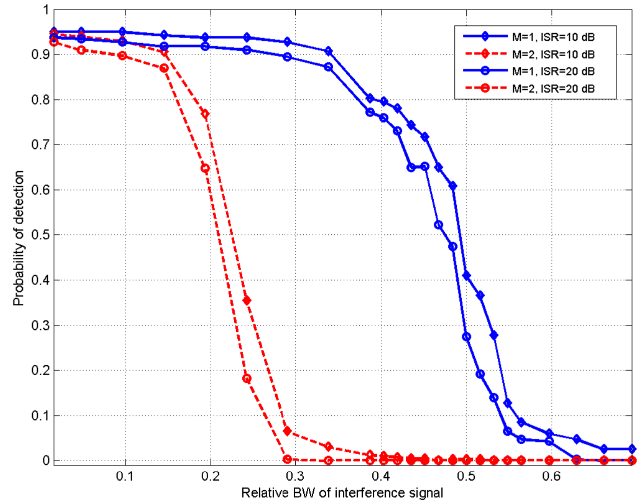

FIGURE 9. Probability of detection versus the relative BW of the interference signal.

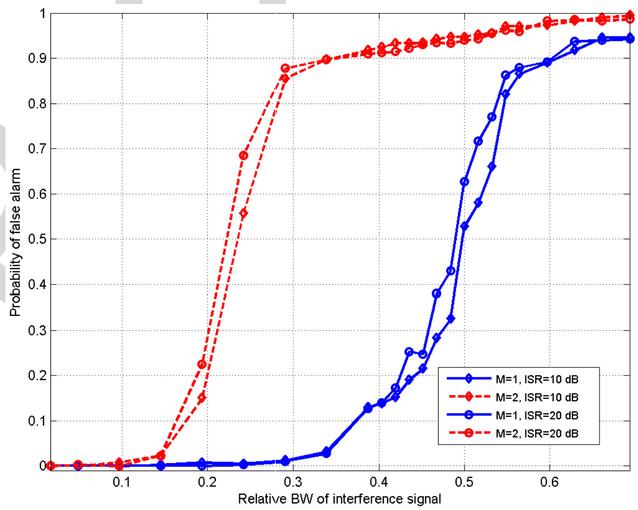

FIGURE 10. Probability of false alarm versus the relative BW of the interference signal.

over more than one third of the BW, the proposed synchronization algorithm cannot effectively cancel the interference signal while preserving the information contained in the PSS. We can also notice from Fig. 9 and Fig. 10 that increasing the number of segments from $M = 1$ to $M = 2$ reduces the interference suppression capability of the proposed algorithm by a factor of two. This can be attributed to the reduced length of the adaptive filters when $M = 2$ that reduces the available degrees of freedom required to place nulls at the frequencies of the interference signal.

Next, we investigate the sensitivity of the proposed algorithm to CFO. Since the proposed algorithm performs CFO estimation after PSS and SSS detection and decoding, its performance can be sensitive to CFO errors. As the CFO increases, the received PSS signal deviates more from the stored PSS signatures and the adaptive filter cancels the

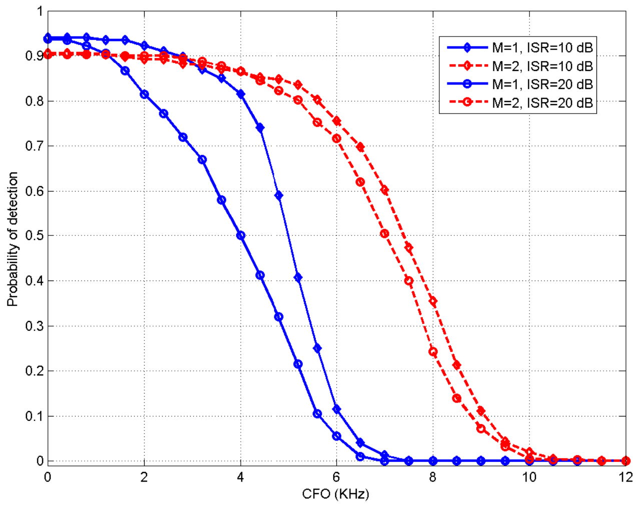

FIGURE 11. Probability of detection versus CFO.

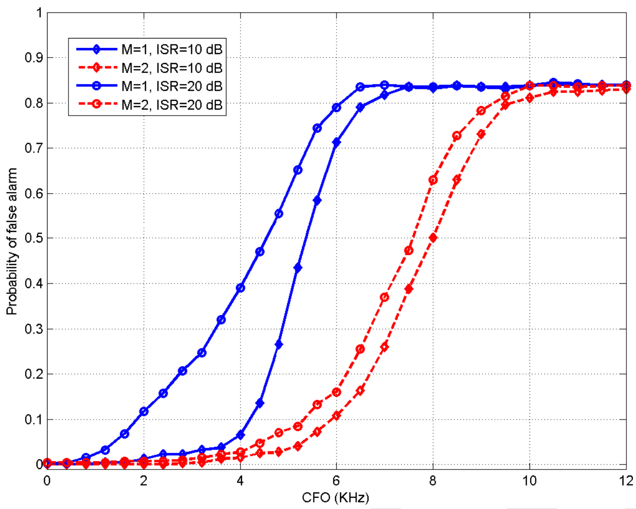

FIGURE 12. Probability of false alarm versus CFO.

PSS signal instead of preserving it. The problem is more pronounced in the presence of strong interference where the adaptive filter places deep nulls at the interference signal frequencies which reduces the contribution of the corresponding subcarriers to the PSS detection metric. Fig. 11 and Fig. 12 respectively show the probabilities of detection and false alarm versus CFO at two values of ISR. We can see from these figures that increasing the number of segments from $M = 1$ to $M = 2$ significantly improves the sensitivity of the algorithm towards CFO due to reducing the maximum deviation from the stored PSS signatures by decreasing the length of the adaptive filter. We can also notice that the sensitivity of the proposed algorithm to CFO increases at higher ISR values. Fig. 13 shows the RMSE in CFO estimate versus CFO computed only over the runs in which correct detection occurred and displayed only when the probability of detection is higher than 0.25. We can see from this figure that the CFO estimate of the proposed algorithm starts to deteriorate as the CFO approaches the detection range of

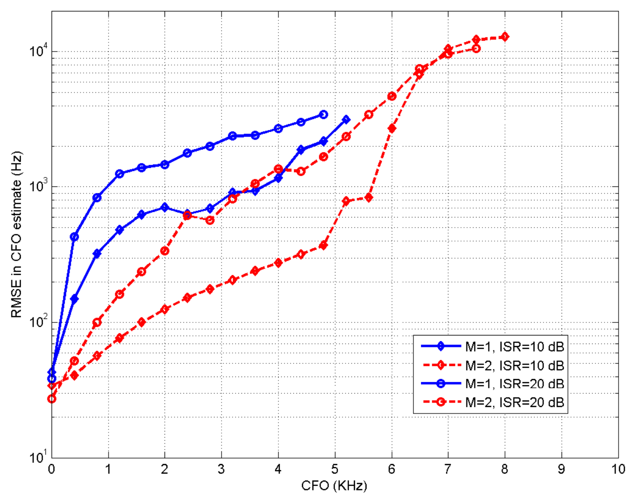

FIGURE 13. RMSE in CFO estimate versus CFO.

the algorithm. We can also see that increasing the number of segments from $M = 1$ to $M = 2$ yields improved robustness against CFO errors.

V. CONCLUSION

A robust synchronization algorithm is presented for LTE systems to detect and eliminate partial-band interference signals via adaptive filtering. The adaptive filter coefficients are designed according to the LCMV design criterion and are updated iteratively using the RLS algorithm. The proposed algorithm utilizes weighted frequency-domain correlation with stored PSS and SSS signatures to detect the cell identity, duplex mode, and CP mode. Weighted frequency domain processing of the received PSS and SSS is also utilized for CFO estimation. Simulation results have been presented to illustrate the superior performance of the proposed algorithm compared to earlier non-robust and robust synchronization algorithms. The proposed algorithm was shown to be able to successfully synchronize to the LTE downlink even in the presence of strong interference signals covering a significant portion of the BW of the LTE synchronization signals.

APPENDIX: EFFECT OF NUMBER OF SEGMENTS ON THE SENSITIVITY TOWARDS CFO MISMATCHES

In order to simplify the analysis, let us consider an additive white Gaussian channel and assume that the received signal does not contain any interference. We can write the mth segment of the $N \times 1$ input signal vector corresponding to the transmission of the PSS from an eNodeB with physical-layer identity i as

$$\boldsymbol{y}_{(m)}(n_P) = e^{j\frac{2\pi\Delta f(m-1)N}{Mf_s}} \boldsymbol{E}\boldsymbol{c}_{(m),i} + \boldsymbol{n}_{(m)} \tag{31}$$

where the matrix $\boldsymbol{E}$ is a diagonal matrix of dimension $\frac{N}{M} \times \frac{N}{M}$ given by

$$\boldsymbol{E} = \mathrm{diag}\left\{1, e^{j\frac{2\pi\Delta f}{f_s}}, \ldots, e^{j\frac{2\pi\Delta f\left(\frac{N}{M}-1\right)}{f_s}}\right\} \tag{32}$$

that models progressive phase shift incurred on the received signal due to CFO Δf Hz and we have assumed without loss of generality that the phase shift due to CFO at the first sample of the PSS is equal to zero. In (31), the $\frac{N}{M} \times 1$ vector $\boldsymbol{n}_{(m)}$ corresponds to the received noise and is modelled as zero-mean with covariance $\sigma^2 \boldsymbol{I}_{\frac{N}{M}}$ and independent of the transmitted LTE downlink signal. The covariance matrix of the vector $\boldsymbol{y}_{(m)}(n_P)$ is given by

$$\boldsymbol{R}_{(m)} = \boldsymbol{E}\boldsymbol{c}_{(m),i}\boldsymbol{c}_{(m),i}^H\boldsymbol{E}^H + \sigma^2 \boldsymbol{I}_{\frac{N}{M}}. \tag{33}$$

The optimal solution of the LCMV problem in (7) can be easily found using the method of Lagrange multipliers and is given by

$$\boldsymbol{g}^{\star}_{(m)}(n_P) = \frac{1}{M}\boldsymbol{R}_{(m)}^{-1}\boldsymbol{C}_{(m)}\left(\boldsymbol{C}_{(m)}^H\boldsymbol{R}_{(m)}^{-1}\boldsymbol{C}_{(m)}\right)^{-1}\boldsymbol{1}_3. \tag{34}$$

In order to investigate the effect of CFO on the performance of the PSS detection algorithm, let us consider the value of PSS detection metric in (16) when the optimal LCMV filter is utilized and the input to the filter consists of the CFO-distorted PSS signature corresponding to physical-layer identity i. We denote this metric by $u_i^{\star}$ where

$$u_i^{\star} = \sum_{m=1}^{M}\left|\boldsymbol{g}^{\star}_{(m)}(n_P)^H\boldsymbol{E}\boldsymbol{c}_{(m),i}\right|. \tag{35}$$

By substituting with (33) in (34) and using the matrix inversion lemma, we can write $u_i^{\star}$ after some mathematical manipulations as

$$u_i^{\star} = \frac{1}{M}\sum_{m=1}^{M}\left|\frac{\sigma^2\boldsymbol{1}_3^T\left(\tilde{\boldsymbol{C}}_{(m)}^H\tilde{\boldsymbol{C}}_{(m)}\right)^{-1}\tilde{\boldsymbol{C}}_{(m)}^H\boldsymbol{c}_{(m),i}}{\sigma^2 + \boldsymbol{c}_{(m),i}^H\boldsymbol{P}^{\perp}_{\tilde{\boldsymbol{C}}_{(m)}}\boldsymbol{c}_{(m),i}}\right| \tag{36}$$

where $\tilde{\boldsymbol{C}}_{(m)} = \boldsymbol{E}^H\boldsymbol{C}_{(m)}$ and $\boldsymbol{P}^{\perp}_{\tilde{\boldsymbol{C}}_{(m)}}$ is the projection matrix on the orthogonal complement of the subspace spanned by the columns of $\tilde{\boldsymbol{C}}_{(m)}$, i.e.,

$$\boldsymbol{P}^{\perp}_{\tilde{\boldsymbol{C}}_{(m)}} = \boldsymbol{I}_{\frac{N}{M}} - \tilde{\boldsymbol{C}}_{(m)}\left(\tilde{\boldsymbol{C}}_{(m)}^H\tilde{\boldsymbol{C}}_{(m)}\right)^{-1}\tilde{\boldsymbol{C}}_{(m)}^H. \tag{37}$$

In the absence of CFO, i.e., when $\boldsymbol{E} = \boldsymbol{I}_{\frac{N}{M}}$, the vector $\boldsymbol{c}_{(m),i}$ lies in the column space of the matrix $\tilde{\boldsymbol{C}}_{(m)}$, and hence, $\boldsymbol{c}_{(m),i}^H\boldsymbol{P}^{\perp}_{\tilde{\boldsymbol{C}}_{(m)}}\boldsymbol{c}_{(m),i} = 0$. In this case, it can be easily verified that $u_i^{\star} = 1$ for all values of M. In the presence of CFO, the quadratic form $\boldsymbol{c}_{(m),i}^H\boldsymbol{P}^{\perp}_{\tilde{\boldsymbol{C}}_{(m)}}\boldsymbol{c}_{(m),i}$ is always greater than zero which leads to decreasing the value of $u_i^{\star}$. The decrement in the value of $u_i^{\star}$ increases as the distance between the vector $\boldsymbol{c}_{(m),i}$ and the columnspace of the matrix $\tilde{\boldsymbol{C}}_{(m)}$ increases. As the number of segments M decreases, the length of each segment increases and the maximum phase shift due to CFO increases as can be seen from (32). As a result, the distance between the vector $\boldsymbol{c}_{(m),i}$ and the columnspace of the matrix $\tilde{\boldsymbol{C}}_{(m)}$ increases with increasing the number of segments which leads to decreasing the detection metric $u_i^{\star}$. Increasing the number of segment improves the robustness of the metric $u_i^{\star}$ towards CFO mismatches. Fig. 14 shows the worst-case

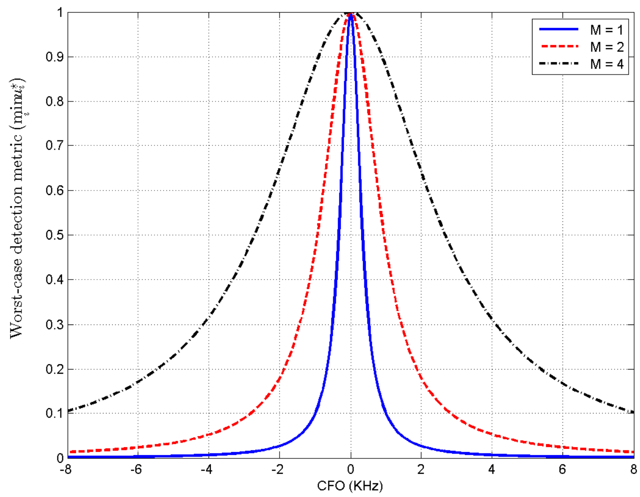

FIGURE 14. Sensitivity of detection metric $u_i^{\star}$ towards CFO for different values of M.

detection metric over all physical-layer identities, i.e., $\min_i u_i^{\star}$ versus CFO for $M = 1, 2, 4$ where the value of σ^2 was selected as 0.1. The improvement in the robustness of the proposed algorithm towards CFO with increasing the number of segments can be clearly seen from Fig. 14.

REFERENCES

[1] S. Sesia, I. Toufik, and M. Baker, *LTE—The UMTS Long Term Evolution: From Theory to Practice*, 2nd ed. New York, NY, USA: Wiley, 2011.

[2] F. Rayal, "LTE in a nutshell: The physical layer," Telesyst. Innov. Inc., Markham, ON, Canada, White Paper TSI 100402-004, 2010.

[3] A. Paulson and T. Schwengler, "A review of public safety communications, from LMR to voice over LTE (VoLT E)," in *Proc. IEEE Symp. Pers., Indoor, Mobile Radio Commun.*, Sep. 2013, pp. 3513–3517.

[4] R. Favraud, A. Apostolaras, N. Nikaein, and T. Korakis, "Toward moving public safety networks," *IEEE Commun. Mag.*, vol. 54, no. 3, pp. 14–20, Mar. 2016.

[5] M. Lauridsen, L. C. Gimenez, I. Rodriguez, T. B. Sorensen, and P. Mogensen, "From LTE to 5G for connected mobility," *IEEE Commun. Mag.*, vol. 55, no. 3, pp. 156–162, Mar. 2017.

[6] T. C. Clancy, M. Norton, and M. Lichtman, "Security challenges with LTE-Advanced systems and military spectrum," in *Proc. IEEE Military Commun. Conf.*, Nov. 2013, pp. 375–381.

[7] X. Li, X. Xie, J. Zeng, and Y. Wang, "Vulnerability analysis and verification for LTE initial synchronization mechanism," in *Proc. IEEE Sarnoff Symp.*, Sep. 2015, pp. 150–154.

[8] M. Lichtman, J. H. Reed, T. C. Clancy, and M. Norton, "Vulnerability of LTE to hostile interference," in *Proc. IEEE Global Conf. Signal Inf. Process. (GlobalSIP)*, Dec. 2013, pp. 285–288.

[9] C. Shahriar *et al.*, "Phy-layer resiliency in OFDM communications: A tutorial," *IEEE Commun. Surveys Tuts.*, vol. 17, no. 1, pp. 292–314, 1st Quart., 2015.

[10] G. Philippe *et al.*, "LTE resistance to jamming capability: To which extend a standard LTE system is able to resist to intentional jammers," in *Proc. Military Commun. Inf. Syst. Conf.*, Oct. 2013, pp. 1–4.

[11] J. P. Miranda, D. Melgarejo, F. Mathilde, R. Yoshimura, F. A. de Figueiredo, and J. J. Bazzo, "Narrowband interference suppression in long term evolution systems," in *Proc. IEEE 25th Annu. Int. Symp. Pers., Indoor, Mobile Radio Commun.*, Sep. 2014, pp. 628–632.

[12] H. J. Kwon *et al.*, "Licensed-assisted access to unlicensed spectrum in LTE release 13," *IEEE Commun. Mag.*, vol. 55, no. 2, pp. 201–207, Feb. 2017.

[13] A. Mukherjee *et al.*, "System architecture and coexistence evaluation of licensed-assisted access LTE with IEEE 802.11," in *Proc. IEEE Int. Conf. Commun. Workshop*, Jun. 2015, pp. 2350–2355.

[14] N. Rupasinghe and I. Güvenç, "Licensed-assisted access for WiFi-LTE coexistence in the unlicensed spectrum," in *Proc. IEEE Globecom Workshops*, Dec. 2014, pp. 894–899.
[15] J. Miloš and S. Hanus, "Performance analysis of PCFICH and PDCCH LTE control channels," in *Proc. Int. Conf. Digit. Telecommun.*, Apr. 2013, pp. 32–37.
[16] T. C. Clancy, "Efficient OFDM denial: Pilot jamming and pilot nulling," in *Proc. IEEE Int. Conf. Commun.*, Jun. 2011, pp. 1–5.
[17] S. Ohno and G. B. Giannakis, "Optimal training and redundant precoding for block transmissions with application to wireless OFDM," in *Proc. IEEE Int. Conf. Acoust., Speech, Signal Process.*, vol. 4. May 2001, pp. 2389–2392.
[18] Z. Zhang, J. Liu, and K. Long, "Low-complexity cell search with fast PSS identification in LTE," *IEEE Trans. Veh. Technol.*, vol. 61, no. 4, pp. 1719–1729, May 2012.
[19] M. Morelli and M. Moretti, "A robust maximum likelihood scheme for PSS detection and integer frequency offset recovery in LTE systems," *IEEE Trans. Wireless Commun.*, vol. 15, no. 2, pp. 1353–1363, Feb. 2016.
[20] M. Labib, V. Marojevic, J. H. Reed, and A. I. Zaghloul, "How to enhance the immunity of LTE systems against RF spoofing," in *Proc. Int. Conf. Comput., Netw. Commun. (ICNC)*, Feb. 2016, pp. 1–5.
[21] H. Minn, V. K. Bhargava, and K. B. Letaief, "A robust timing and frequency synchronization for OFDM systems," *IEEE Trans. Wireless Commun.*, vol. 2, no. 4, pp. 822–839, Jul. 2003.
[22] M. Marey and H. Steendam, "Analysis of the narrowband interference effect on OFDM timing synchronization," *IEEE Trans. Signal Process.*, vol. 55, no. 9, pp. 4558–4566, Sep. 2007.
[23] S. Aghajeri and H. Shafiee, "Synchronization in OFDM powerline communication systems in presence of narrowband interferences," in *Proc. Int. Symp. Signal Process. Appl.*, vol. 2. Jul. 2003, pp. 359–362.
[24] J.-I. Kim, J.-S. Han, H.-J. Roh, and H.-J. Choi, "SSS detection method for initial cell search in 3GPP LTE FDD/TDD dual mode receiver," in *Proc. Int. Symp. Commun. Inf. Technol.*, Sep. 2009, pp. 199–203.
[25] Y. Yu and Q. Zhu, "A novel time synchronization for 3GPP LTE cell search," in *Proc. Int. ICST Conf. Commun. Netw. China*, Aug. 2013, pp. 328–331.
[26] X. Yang, Y. Xiong, G. Jia, W. Fang, and X. Zheng, "PSS based time synchronization for 3GPP LTE downlink receivers," in *Proc. IEEE Int. Conf. Commun. Technol.*, Sep. 2011, pp. 930–933.
[27] B. M. Popovic and F. Berggren, "Primary synchronization signal in E-UTRA," in *Proc. IEEE Int. Symp. Spread Spectrum Techn. Appl.*, Aug. 2008, pp. 426–430.
[28] H. Setiawan and H. Ochi, "A low complexity physical-layer identity detection for 3GPP long term evolution," in *Proc. Int. Conf. Adv. Commun. Technol.*, vol. 1. Feb. 2010, pp. 8–13.
[29] Y. Gao, G. Zhu, X. Chen, D. Wu, and B. Ban, "A modified algorithm of synchronization signal detection for LTE initial cell search," in *Proc. Int. ICST Conf. Commun. Netw. China*, Aug. 2011, pp. 1211–1215.
[30] K. Manolakis, D. M. G. Estevez, V. Jungnickel, W. Xu, and C. Drewes, "A closed concept for synchronization and cell search in 3GPP LTE systems," in *Proc. IEEE Wireless Commun. Netw. Conf.*, Apr. 2009, pp. 1–6.
[31] H. G. Park, I. K. Kim, and Y. S. Kim, "Efficient coherent neighbour cell search for synchronous 3GPP LTE system," *Electron. Lett.*, vol. 44, no. 21, pp. 1267–1268, Oct. 2008.
[32] Y.-L. Shi, P.-L. Shui, and Y.-B. Zhao, "Oversampling gain in adaptive normalised matched filter detector," *IET Radar, Sonar, Navigat.*, vol. 5, no. 9, pp. 987–993, Dec. 2011.
[33] B. R. Breed and J. Strauss, "A short proof of the equivalence of LCMV and GSC beamforming," *IEEE Signal Process. Lett.*, vol. 9, no. 6, pp. 168–169, Jun. 2002.
[34] P. H. Moose, "A technique for orthogonal frequency division multiplexing frequency offset correction," *IEEE Trans. Commun.*, vol. 42, no. 10, pp. 2908–2914, Oct. 1994.
[35] S. Huang, Y. Su, Y. He, and S. Tang, "Joint time and frequency offset estimation in LTE downlink," in *Proc. Int. ICST Conf. Commun. Netw. China*, Aug. 2012, pp. 394–398.
[36] R. Krenz and S. Brahma, "Jamming LTE signals," in *Proc. IEEE Int. Black Sea Conf. Commun. Netw.*, May 2015, pp. 72–76.
[37] T. Li, W. H. Mow, V. K. N. Lau, M. Siu, R. S. Cheng, and R. D. Murch, "Robust joint interference detection and decoding for OFDM-based cognitive radio systems with unknown interference," *IEEE J. Sel. Areas Commun.*, vol. 25, no. 3, pp. 566–575, Apr. 2007.
[38] J. Tan and G. L. Stuber, "Multicarrier spread spectrum system with constant envelope: Antijamming, jamming estimation, multiuser access," *IEEE Trans. Wireless Commun.*, vol. 4, no. 4, pp. 1527–1538, Jul. 2005.
[39] D. W. Chi and P. Das, "Effect of jammer on the performance of OFDM in the presence of nonlinearity in Rayleigh fading channel with application to 802.11n WLAN," in *Proc. IEEE Military Commun. Conf.*, Oct. 2006, pp. 1–7.

AMR EL-KEYI received the B.Sc. and M.Sc. degrees in electrical engineering from Alexandria University in 1999 and 2002, respectively, and the Ph.D. degree in electrical engineering from McMaster University, Hamilton, ON, Canada, in 2006. He was a Post-Doctoral Research Fellow with the Department of Electrical and Computer Engineering, McGill University, from 2007 to 2008. In 2009, he joined the School of Communication and Information Technology, Nile University, as an Assistant Professor and was promoted to an Associate Professor in 2015. In 2015, he joined Carleton University as a Visiting Scientist in fifth generation wireless networks. He is currently with Ericsson, Ottawa, ON, Canada, as a System Design Engineer. He has authored over 80 refereed conference and journal publications. His research interests include array processing and adaptive beamforming, cognitive radio, channel modeling and estimation, and interference management for wireless communication systems.

OKTAY ÜRETEN received the Ph.D. degree in electronics engineering from the University of Ankara, Ankara, Turkey, in 2000. He was a Lecturer with the Electronics Engineering Department, University of Ankara, and a Senior Researcher with the National Research Institute of Electronics and Cryptology, Turkey, from 2000 to 2001. From 2001 to 2012, he was a Research Scientist with the Radio Communication Technologies Research Group, Communications Research Centre, Ottawa, ON, Canada, where he was involved in various projects in military radio communications and signal processing. He is currently with Allen-Vanguard Corporation, Ottawa, where he is involving in developing algorithms for the current and next generation electronic warfare platforms of the company. He has authored over 30 journal and conference papers in signal processing and radio communications. He holds patents.

Dr. Üreten has served as a TPC member and a reviewer of the IEEE conferences and journals. He holds two best paper awards from the IEEE.

HALIM YANIKOMEROGLU (F'17) was born in Giresun, Turkey, in 1968. He received the B.Sc. degree in electrical and electronics engineering from Middle East Technical University, Ankara, Turkey, in 1990, and the M.A.Sc. degree in electrical engineering and the Ph.D. degree in electrical and computer engineering from the University of Toronto, Toronto, ON, Canada, in 1992 and 1998, respectively. From 1993 to 1994, he was with the Research and Development Group, Marconi Kominikasyon A.S., Ankara. He spent the 2011–2012 academic year with the TOBB University of Economics and Technology, Ankara, as a Visiting Professor. Since 1998, he has been with the Department of Systems and Computer Engineering, Carleton University, Ottawa, ON, Canada, where he is currently a Full Professor. His research interests include wireless technologies with a special emphasis on wireless networks. In recent years, his research has been funded by Huawei, Telus, Allen Vanguard, Mapsted, Blackberry, Samsung, Communications Research Centre of Canada, and DragonWave. This collaborative research resulted in over 30 patents (granted and applied). He was a recipient of the IEEE Ottawa Section Outstanding Educator Award in 2014, the Carleton University Faculty Graduate Mentoring Award in 2010, the Carleton University Graduate Students Association Excellence Award in Graduate Teaching in 2010, and the Carleton University Research Achievement Award in 2009. He is a Distinguished Lecturer for the IEEE Communications Society and a Distinguished Speaker for the IEEE Vehicular Technology Society. He is a Registered Professional Engineer in the province of Ontario, Canada. He has been involved in the organization of the IEEE Wireless Communications and Networking Conference (WCNC) from its inception, including serving as a Steering Committee Member and the Technical Program Chair or the Co-Chair of WCNC 2004 (Atlanta, GA, USA), WCNC 2008 (Las Vegas, NV, USA), and WCNC 2014 (Istanbul, Turkey). He was the General Co-Chair of the IEEE Vehicular Technology Conference (VTC) 2010-Fall held in Ottawa. He is serving as the General Chair of IEEE VTC 2017-Fall, Toronto. He has served on the editorial boards of the IEEE Transactions on Communications, the IEEE Transactions on Wireless Communications, and the IEEE Communications Surveys and Tutorials. He was the Chair of the IEEE Technical Committee on Personal Communications (now called Wireless Technical Committee).

TREVOR YENSEN received the M.Eng. and Ph.D. degrees in electrical engineering from Carleton University in Ottawa, ON, Canada, in 2003 and 1998, respectively. He was with Allen Vanguard Corporation to establish a world-class electronic warfare (EW) program, with a focus on jamming systems for remote control improvised explosive devices, over the past 13 years. As the Chief Scientist with Allen Vanguard, he focused on enhancing EW technology through in-house development and partnerships, including collaborations with academia.

He has many conference and journal publications and patents in wireless communications and acoustic signal processing.